The Astrophysical Journal Letters, 916:L21 (9pp), 2021 August 1 https://doi.org/10.3847/2041-8213/ac12cc

Turbulent Acceleration of Interstellar Pickup Ions at the Heliospheric Termination Shock Forms the Global ENA Spectrum

E. J. Zirnstein[1], R. Kumar[2], R. Bandyopadhyay[1], M. A. Dayeh[3,4], J. Heerikhuisen[5], and D. J. McComas[1]
[1] Department of Astrophysical Sciences, Princeton University, Princeton, NJ 08544, USA; ejz@princeton.edu
[2] Princeton Plasma Physics Laboratory, Princeton University, Princeton, NJ 08543, USA
[3] Southwest Research Institute, San Antonio, TX 78228, USA
[4] Department of Physics and Astronomy, University of Texas at San Antonio, San Antonio, TX 78249, USA
[5] Department of Mathematics and Statistics, University of Waikato, Hamilton, New Zealand
Received 2021 April 22; revised 2021 June 17; accepted 2021 July 8; published 2021 August 3

Abstract

The heliospheric energetic neutral atom spectrum observed by the Interstellar Boundary Explorer (IBEX) reveals that the heliosheath proton distribution is consistent with a power law. The origin of the spectrum is likely from interstellar pickup ions (PUIs) accelerated at the heliospheric termination shock (HTS). We present an explanation of the proton spectrum origin using a test particle simulation of PUIs accelerated at the HTS. PUIs experience preferential heating by the motional electric field in the shock foot, but do not develop a power-law tail without the presence of turbulence at wavenumbers (k) close to the PUI gyroradius scale (R_g). Voyager 2 observations of the magnetic field downstream of the HTS indicate a moderate amount of turbulence at $kR_g \cong 1$, $(\delta B/B_0)^2 \cong 0.01$, which we find to be sufficient for producing a downstream suprathermal PUI tail but not at intensities observed by IBEX. Within the shock ramp, however, Voyager observed the turbulence power at much smaller scales to be nearly 100 times stronger, suggesting the possibility of strong turbulence at the PUI gyroradius scale. We show that a proton distribution can develop a power law downstream of the HTS consistent with IBEX observations if $(\delta B/B_0)^2 \gtrsim 0.1$ at $kR_g \cong 1$ in the shock foot. Shock drift acceleration of PUIs by the motional electric field is aided by interactions with turbulence upstream of the shock overshoot. Steepening of the IBEX proton spectrum in directions farther from the heliospheric nose suggests the HTS compression ratio and/or turbulence power weakens near the heliotail.

Unified Astronomy Thesaurus concepts: Heliosheath (710); Pickup ions (1239); Solar wind (1534); Termination shock (1690); Space plasmas (1544); Interplanetary turbulence (830); Interplanetary particle acceleration (826)

1. Introduction

The solar wind (SW) flowing out from the Sun fills interplanetary space with plasma consisting mostly of protons, electrons, and alpha particles, and a frozen-in magnetic field (Parker 1958). Interstellar neutral atoms ionized by charge-exchange or photoionization are regularly picked up by the SW, forming a nonthermal distribution of interstellar "pickup ions" (PUIs) with a relatively high mean energy ($>10^6$ K; McComas et al. 2017). PUIs initially form unstable ring distributions in the plasma frame and quickly scatter in pitch angle onto filled shell distributions—a process that subsequently generates turbulence and heats the SW (Richardson & Smith 2003; Isenberg 2005; Zank et al. 2018). Observations of interstellar PUIs in the outer heliosphere have been made uniquely by the Solar Wind Around Pluto (SWAP) instrument on board New Horizons, and reveal that PUIs dominate the internal pressure of the SW plasma beyond ~20 au from the Sun (McComas et al. 2017, 2021). PUIs are preferentially accelerated at interplanetary shocks (Zirnstein et al. 2018b), and they mediate the heliospheric termination shock (HTS) interaction (Zank et al. 1996; Richardson et al. 2008; Matsukiyo & Scholer 2014; Yang et al. 2015; Kumar et al. 2018). Thus, the ubiquitous presence of PUIs in the heliosphere is a topical subject of research for the heliospheric community.

PUI acceleration at the HTS is important for understanding the origin of anomalous cosmic rays (ACRs; Chalov 2005; McComas & Schwadron 2006; Decker et al. 2008; Senanayake & Florinski 2013; Giacalone et al. 2021), the distribution of plasma pressure in the inner heliosheath (IHS) beyond the HTS (Fahr & Siewert 2013; Livadiotis et al. 2013; Schwadron et al. 2014), and the emission of energetic neutral atoms (ENAs) from the boundary regions of the heliosphere (Desai et al. 2019; Reisenfeld et al. 2019; McComas et al. 2020). The Interstellar Boundary Explorer (IBEX; McComas et al. 2009) measures H ENAs between ~0.1 and 6 keV FWHM, observing the spectrum of ENAs produced by charge-exchange between interstellar neutral atoms and PUIs accelerated at the HTS.

In this Letter, we present a model of PUI acceleration at the HTS that yields a downstream proton distribution consistent with proton spectra derived from IBEX ENA observations. Voyager 2 observations (Burlaga et al. 2008; Richardson et al. 2008) and results from a fully kinetic, particle-in-cell (PIC) simulation (Kumar et al. 2018) are used to constrain our model. We show that the presence of significant turbulence near the HTS leads to stochastic shock drift acceleration of PUIs in the shock foot and ramp, which produces a suprathermal tail downstream of the HTS.

2. Model Description

We simulate the acceleration of protons from the SW (hereafter called SW ions, or SWIs) and PUIs at the HTS using the test particle approach (Zirnstein et al. 2020). We initialize a large number of "weighted" particles ($\sim 2.9 \times 10^6$) with

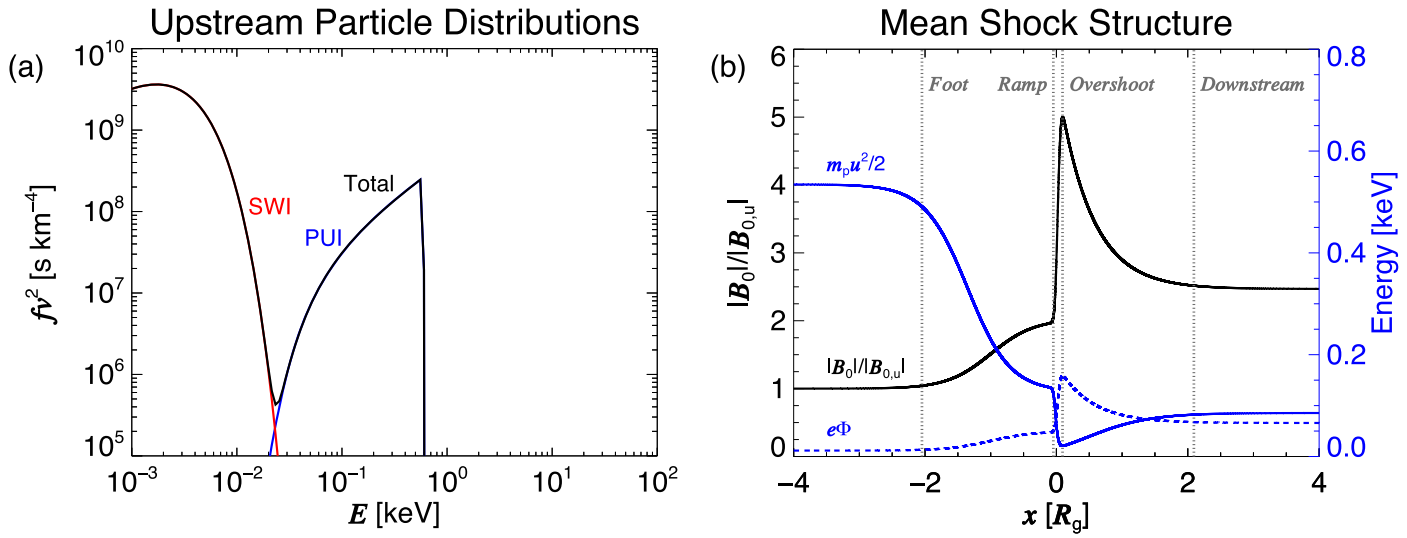

Figure 1. (a) Upstream particle energy distribution in the plasma frame. (b) Mean shock profile (bulk flow kinetic energy, mean magnetic field, cross-shock potential) at the HTS. B_0 represents the local mean field, and $B_{0,u}$ is the upstream field.

collective properties mimicking the upstream proton distribution and distributed with equal number of particles per logarithmic speed bin. The weight of each particle represents a section of the speed distribution function given by $f(v)v^2dv$, where v is the particle speed in the plasma frame, $f(v) = (1-\alpha)f_{\rm SWI}(v) + \alpha f_{\rm PUI}(v)$ is the upstream distribution function of SWIs and PUIs with relative PUI density fraction $\alpha = 0.25$ (McComas et al. 2021), and dv is the bin size at speed v. We assume that the SWI distribution $f_{\rm SWI}(v)$ is Maxwell–Boltzmann with a temperature of 20,000 K (Richardson et al. 2008), and the PUI distribution $f_{\rm PUI}(v)$ is a filled shell. We use a generalized filled shell distribution based on New Horizons's SWAP observations (McComas et al. 2021), which revealed that PUIs undergo nonadiabatic heating via interactions with turbulence and/or shocks far from the Sun. The PUI cooling index, which equals 1.5 for adiabatic cooling, is set to 2.9 in our model based on extrapolation of SWAP PUI measurements to the HTS. Voyager 2 observed that the SW speed was 320 km s^{-1} upstream of the HTS (Richardson et al. 2008). The PUI filled shell cutoff speed is determined by the relative SW velocity and interstellar neutral H velocity ($u_{\rm H} \cong 15$ km s^{-1}; Heerikhuisen et al. 2016). Therefore, we assume that the PUI filled shell cutoff is $u_c = 335$ km s^{-1}. The upstream proton distribution is shown in Figure 1(a).

The upstream velocity distribution is isotropic in the plasma frame, where particles are initially positioned randomly in the ranges $-154R_g < x < -4R_g$, $|y| < 75R_g$, and $|z| < 75R_g$, where R_g is the upstream ion advective gyroradius and the shock ramp is located at $x = 0$. The bulk plasma flows toward the HTS in the $+x$ direction, the shock normal points toward $-x$, and the mean magnetic field lies in the x–y plane.

The test particles' trajectories are evolved by solving the nonrelativistic Lorentz force equation,

$$\frac{d\boldsymbol{v}}{dt} = \frac{e}{m}(\boldsymbol{E} + \boldsymbol{v} \times \boldsymbol{B}), \tag{1}$$

using the Bulirsch–Stoer method with adaptive stepping (Press et al. 2002), where m is proton mass, e is charge, $\boldsymbol{B} = \boldsymbol{B}_0 + \delta\boldsymbol{B}$ is the total magnetic field, $\boldsymbol{B}_0$ is the mean magnetic field (Figure 1(b)), $\delta\boldsymbol{B}$ is the turbulent magnetic field (Figure 2), $\boldsymbol{E}$ is the electric field given as

$$\boldsymbol{E} = -\boldsymbol{u} \times \boldsymbol{B} - \nabla\Phi, \tag{2}$$

and $\boldsymbol{u}$ is the prescribed bulk flow velocity. The cross-shock potential (CSP), Φ, is derived from the electron momentum equation (Leroy 1983),

$$e\Phi(x) = e\int_{-\infty}^{x} u_z(x')B(x')dx' + \frac{\gamma}{\gamma-1}k_B T_e(x) + \frac{B_u}{\mu_0 n_u}(B_y(x) - B_{0,u,y}), \tag{3}$$

where $\gamma = 5/3$, $B_{0,u} = 0.05$ nT is the upstream mean magnetic field magnitude, $n_u = 0.0013$ cm^{-3} is the upstream plasma density, and T_e is electron temperature. The Alfvén Mach number upstream of the HTS is ~10.7. Particles are tracked from their initial position to a region downstream of the HTS where they are binned into a distribution function (see Appendix C).

A detailed description of the mean and turbulent magnetic fields utilized in our model is presented in Appendix A. The mean magnetic field $\boldsymbol{B}_0$, shown in Figure 1(b), includes a PUI foot, ramp, overshoot, and downstream region that are each scaled to approximately reproduce Voyager 2 observations of the HTS. We note that while a separate SWI foot likely exists ahead of the ramp and is coupled to the shock self-reformation process (Matsukiyo & Scholer 2014; Lembège & Yang 2016), it does not significantly affect the transport of PUIs due to its relatively small size. A description of the CSP energy derived from Voyager 2 observations and PIC simulation results is given in Appendix B.

Turbulence in the vicinity of the HTS is a superposition of upstream SW turbulence processed through the HTS and locally generated fluctuations due to the particle phase space anisotropies at the HTS. To determine the most realistic spectrum of turbulence to apply in our model, we analyze Voyager 2 high-resolution (0.48 s) magnetic field measurements of the third crossing of the HTS (Burlaga et al. 2008), shown in Figure 2. We calculate the

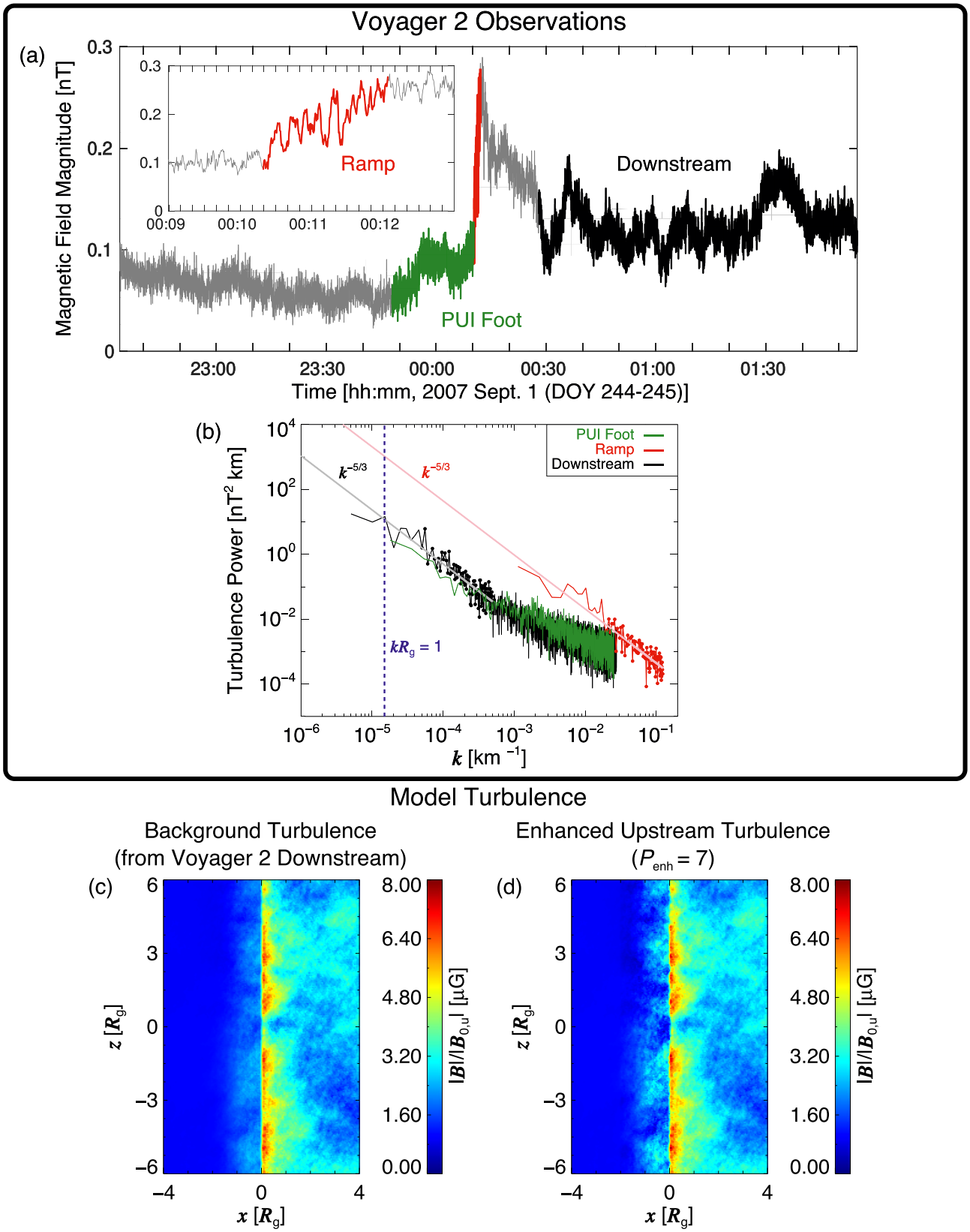

Figure 2. Voyager 2 observations of magnetic field at the HTS (third crossing; Burlaga et al. 2008). (b) Turbulence power spectra in the PUI foot (green), ramp (red), and downstream (black) regions. The ramp and downstream spectra are reasonably fit by a Kolmogorov (k-$^{5/3}$) spectrum and differ by almost 2 orders of magnitude in power. The downstream spectrum is fit over $k = [5 \times 10^{-5}, 5 \times 10^{-4}]$ km^{-1}, and the ramp spectrum is fit over $k = [2 \times 10^{-2}, 1 \times 10^{-1}]$ km^{-1}. The wavenumber at the upstream PUI gyroradius scale is shown in blue. (c) Model turbulence using Voyager 2 observations downstream of the shock ("background turbulence"), and (d) turbulence power enhanced in the PUI foot and ramp by a factor $P_{\rm enh}$.

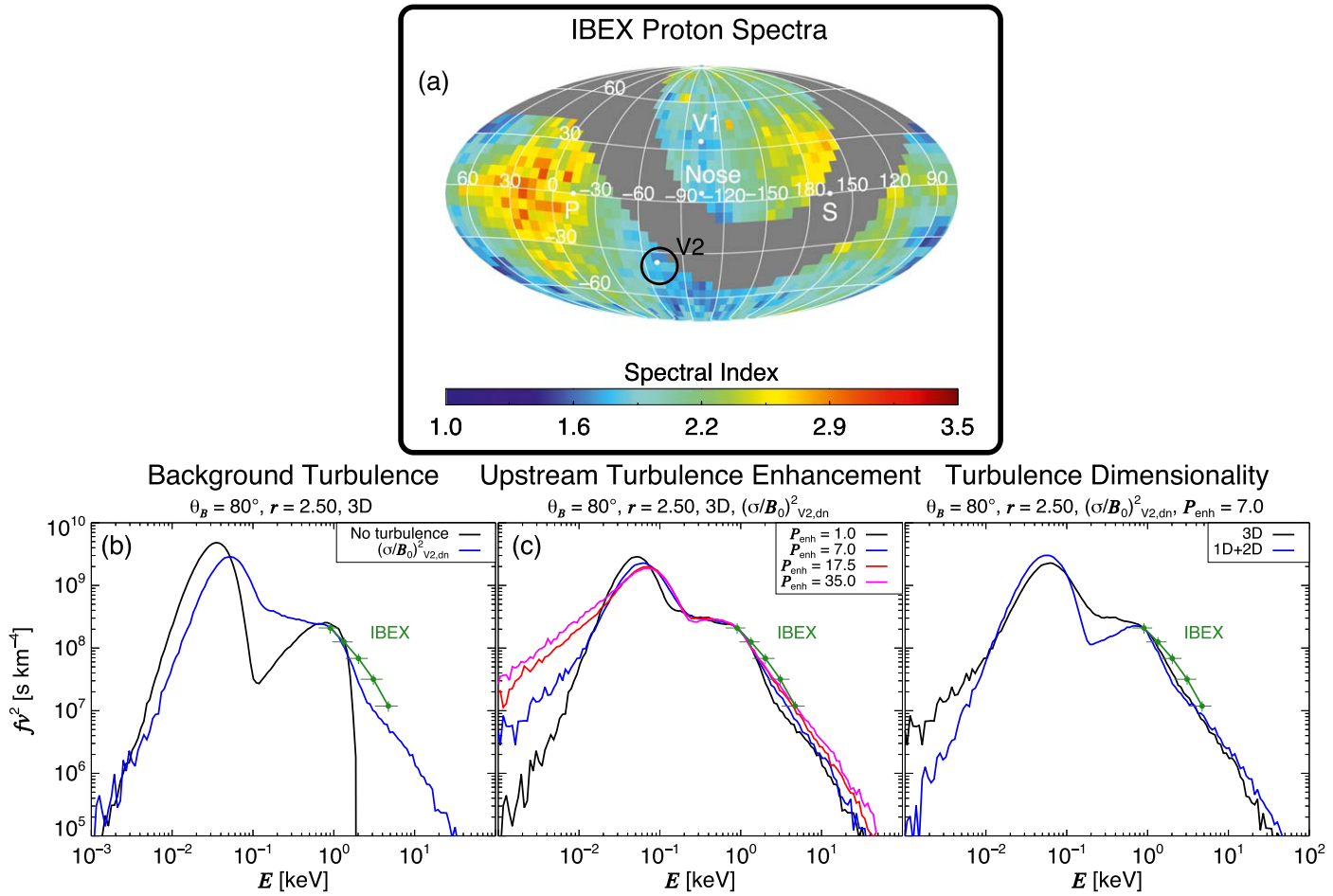

Figure 3. (a) All-sky map of IBEX proton spectral indices in the IHS plasma frame (Zirnstein et al. 2021). IBEX proton fluxes from the direction of Voyager 2 (V2) are shown in green in panels (b)–(d). We show simulated proton distributions downstream of the shock as a function of (b) background turbulence (equal to V2 downstream turbulence), (c) turbulence enhancement, and (d) turbulence dimensionality. All results with turbulence in panels (b) and (c) assume 3D isotropic turbulence. 1D+2D turbulence in panel (d) is a composite of 10% 1D and 90% 2D turbulence.

turbulence power spectra in three regions (Figure 2(b)). The turbulence power spectrum in the downstream region extends up to the PUI gyroradius scale and is consistent with a Kolmogorov $-5/3$ scaling (Kolmogorov 1941; Matthaeus & Goldstein 1982). The turbulence power ratio (the squared ratio of turbulent magnetic field, δB, to mean magnetic field, B_0) at $kR_g = 1$ is $(\delta B/B_0)^2 \cong 0.01$. We use this level of turbulence power as the "background turbulence" in our test particle model (see Appendix A). The turbulence power in the ramp of the HTS, while only quantifiable at scales $<0.01R_g$, is almost 100 times higher than the downstream turbulence power if extrapolated to similar wavenumbers. On the other hand, the level of turbulence at $kR_g \cong 1$ in the PUI foot may not be distinctly identified from the observations since the size of fluctuations, whose amplitude is modulated along Voyager 2's trajectory, is comparable to the foot width. From the green curve in Figure 2(b), only the very lowest wavenumber modes of the PUI foot spectrum resolve length scales close to $kR_g \cong 1$. Because the low-wavenumber modes in a Fourier spectrum have low statistical weight (Matthaeus & Goldstein 1982), the level of turbulence at $kR_g \cong 1$ in the PUI foot may not be accurately estimated from the observations. Moreover, a single sampling of magnetic field along the shock normal is inadequate at determining turbulence anisotropy. In Section 3, we show that an enhancement of turbulence or waves near $kR_g \cong 1$ is necessary to accelerate PUIs to fluxes observed by IBEX.

3. Results

The acceleration of PUIs at the quasi-perpendicular HTS has been studied in detail before, but the presence of strong turbulence power at the PUI gyroradius scale and its connection to IBEX observations have not been considered. Global observations of ENAs by IBEX reveal that the IHS proton distribution is power-law-like in the energy range ~0.7–7 keV in the downstream plasma frame (Zirnstein et al. 2021; Figure 3(a)). Since IBEX observations are a line-of-sight integration of ENA sources, the observations represent the mean proton distribution in the IHS. It is possible that protons experience a certain amount of energy diffusion via interactions with shocks or turbulence (Zirnstein et al. 2018a; Mostafavi et al. 2019) and modification by charge-exchange (Zirnstein & McComas 2015) as they propagate through the IHS. In this study, we assume that changes to the proton distribution through the IHS are negligible. We examine this assumption in more detail in Section 4.

3.1. Enhanced Turbulence in the Shock Foot Forms the IBEX Proton Spectrum

Figure 3 shows the main results of our study. We compare our model proton fluxes to IBEX proton fluxes derived by Zirnstein et al. (2021), where the observed fluxes were calculated assuming

an IHS thickness in the Voyager 2 direction of 35 ± 5 au (Stone et al. 2019) and interstellar neutral H density of $0.127 \pm 0.015\,\mathrm{cm}^{-3}$ (Swaczyna et al. 2020). Without turbulence, the PUI filled shell is compressed and heated but exhibits a steep rollover between ~1 and 2 keV. With a small level of "background" turbulence consistent with Voyager 2 observations downstream of the HTS, defined as $(\sigma/B_0)^2 = (\sigma/B_0)^2_{\mathrm{V2,dn}} = 0.01$ (where σ^2 is the model turbulence variance), the proton spectrum between ~0.1 and 1 keV is filled in and PUIs develop a steep and low-intensity tail above 2 keV (Figure 3(b)). This level of turbulence, however, is insufficient to accelerate PUIs to flux levels observed by IBEX.

Figure 3(c) shows simulation results where we enhanced the turbulence power by a factor P_{enh} in the shock foot and ramp, as described in Appendix A. In this case, PUIs develop a power-law tail above 1 keV that is consistent with IBEX observations when $P_{\mathrm{enh}} \gtrsim 7$. This corresponds to $(\sigma/B_0)^2 \gtrsim 0.1$ at $kR_{\mathrm{g}} = 1$. Incidentally, this level of turbulence power is plausible from Voyager observations, in that if we extend the $-5/3$ fit in the ramp spectra up to $kR_{\mathrm{g}} = 1$, the intercept gives a power level consistent with $P_{\mathrm{enh}} \cong 90$. For $P_{\mathrm{enh}} > 17.5$, the PUI spectrum in the IBEX-Hi energy range converges, but the proton flux increases dramatically above ~10 keV. We note that our model results for $P_{\mathrm{enh}} = 7$ are also consistent with ~40–60 keV ACR fluxes observed by Voyager 2 downstream of the HTS (Decker et al. 2008; Giacalone & Decker 2010). The maximum wavelength of turbulence in our model is $\sim 60R_{\mathrm{g}}$, which appears sufficient to accelerate PUIs up to ~60 keV when $P_{\mathrm{enh}} \cong 7$.

Our model results thus far assumed that turbulence is isotropic and homogeneous, with equal power in fluctuations in all three components of $\delta\boldsymbol{B}$ (Giacalone & Jokipii 1999). It is not clear if this is a realistic portrayal of turbulence in the vicinity of the HTS that may be predominantly produced by particles reflected from the shock. Therefore, Figure 3(d) shows results obtained using a composition of 1D or "slab" turbulence (with $\boldsymbol{k} \| \boldsymbol{B}_0$ and $\delta\boldsymbol{B} \perp \boldsymbol{B}_0$) and 2D "structures" (with $\boldsymbol{k} \perp \boldsymbol{B}_0$ and $\delta\boldsymbol{B} \perp \boldsymbol{B}_0$) (Matthaeus et al. 1990; Bieber et al. 1996), with 10% and 90% of the turbulence power in 1D and 2D waves, respectively. The downstream proton distributions are similar for 3D and 1D+2D turbulence at energies ~1–7 keV, although PUIs are more efficiently accelerated to higher energies in 2D-dominated turbulence. SWIs experience more scattering and heating in 3D turbulence due to fluctuations parallel to $\boldsymbol{B}_0$. For both cases, however, an enhancement of turbulence upstream of the shock overshoot is still required to reproduce IBEX observations.

3.2. Particle Trajectories and Shock Drift Acceleration

The development of a suprathermal PUI tail is a result of stochastic acceleration by the motional electric field upstream of the HTS. This is illustrated in Figures 4 and 5 for the case where $P_{\mathrm{enh}} = 7$. Figure 4 shows examples of PUI trajectories in the vicinity of the HTS (panels (c) and (d)), the mean number of "shock drift gyrations" that particles undergo before finally drifting downstream (panel (a)) and the mean rate of work by the motional electric field that signifies the amount of acceleration experienced by particles forming the downstream distribution. We define a shock drift gyration as the number of times a particle reverses velocity along the shock normal between the PUI foot and overshoot, before going downstream. Above ~0.4 keV, where PUIs dominate the proton spectrum, the mean number of drift gyrations as a function of energy, $\langle N_{\mathrm{d}} \rangle$, exceeds 1 and exponentially increases with energy. Within the IBEX-Hi energy range, the number of shock drift gyrations is $1 < \langle N_{\mathrm{d}} \rangle < 7$. Particles that experience several gyrations or more in the shock front and gain energy in the motional electric field are, by definition, undergoing shock drift acceleration (Armstrong et al. 1985). The presence of turbulence enables some particles to drift along the shock surface for larger periods of time before crossing downstream (Figure 4(a)). We also show the case with no turbulence (dashed curve), where no particles experience preferential acceleration to energies $\gtrsim$2 keV. Figure 4(b) shows that during shock drift, the motional electric field preferentially accelerates PUIs that form the downstream suprathermal tail. A few PUI trajectories are shown in Figures 4(c) and (d). PUIs are able to interact with relatively large amplitude turbulent fluctuations, as compared to SWIs, due to their larger gyroradii. Enhanced pitch angle scattering allows some PUIs to undergo multiple gyrations in the foot/ramp region at the shock (Figure 4(d)).

3.3. Energy Gain in the Motional Electric Field Enabled by Turbulence

Figure 5(a) shows the mean energy of SWIs and PUIs in the plasma frame (i.e., second moment of the local proton distribution) as a function of distance along the shock normal. PUIs gain a significant amount of energy across the HTS in the plasma frame (~0.7 keV), whereas SWIs gain less energy (~0.1 keV). The reason for this difference is the relatively large difference in gyroradius of PUIs versus SWIs.

Next, we quantify the mechanism by which the suprathermal PUI tail develops downstream of the HTS. PUIs reflected upstream of the shock overshoot preferentially gain energy in the upstream motional electric field before they cross downstream (Matsukiyo & Scholer 2014; Yang et al. 2015; Kumar et al. 2018). PUI reflection and acceleration is generally described either as shock drift acceleration (SDA) or shock surfing acceleration (SSA). SDA primarily occurs when particles are reflected and trapped upstream of the shock overshoot by the Lorentz force. SSA occurs when particles are trapped upstream by the CSP. Following Lever et al. (2001) and Yang et al. (2011), we determine which mechanism is responsible for creation of the suprathermal PUI tail downstream of the HTS by tracking the contributions of the CSP electric field, E_x, versus the Lorentz force field, $v_y B_z - v_z B_y$, experienced by each particle along the shock normal. We integrate these two field terms separately over the course of each particle trajectory, but only when (1) the fields are negative, (2) the particle is upstream of the overshoot, and (3) only for particles that reflect at least once upstream of the overshoot. Then, we calculate the ratio $\Gamma = \int E_x dt \Big/ \int (v_y B_z - v_z B_y) dt$ for each particle and compute the weighted mean of this ratio over all particles per energy bin of the downstream distribution function. The relative contributions of SDA and SSA are calculated as $1/(\Gamma + 1)$ and $1 - 1/(\Gamma + 1)$, respectively, and are shown in Figure 5(b). It is clear that SDA is the primary mechanism by which PUIs are able to accelerate at the HTS in our model, contributing to >90% of the downstream PUI distribution.

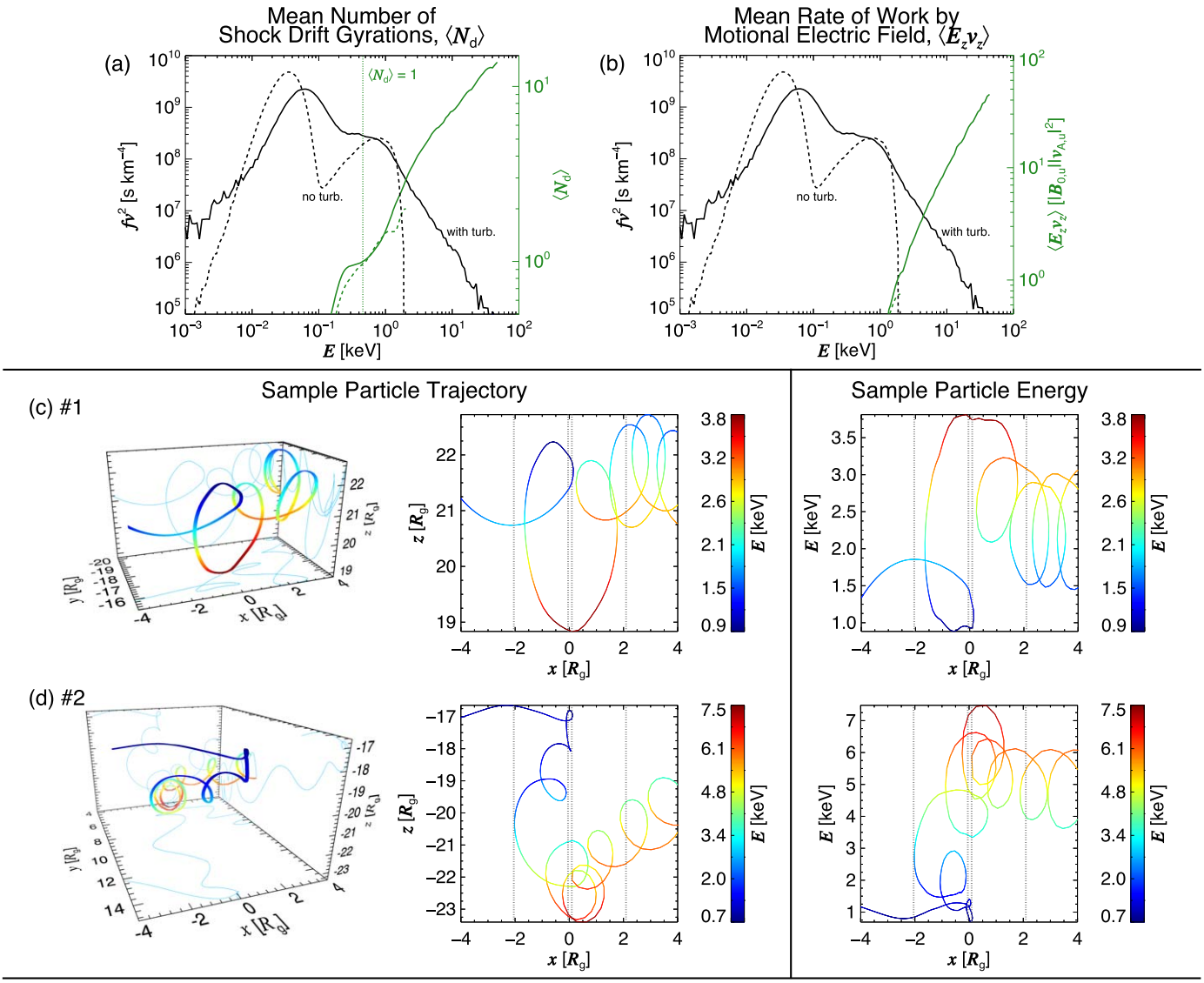

Figure 4. (a) Mean number of "shock drift gyrations," $\langle N_d \rangle$, per energy bin of the downstream distribution in the presence of turbulence. The case with no turbulence is also shown (dashed lines). (b) Mean rate of work by the motional electric field with and without turbulence. Sample particle trajectories and their evolution in energy (in the shock frame) are shown in panel rows (c) and (d). The particle energy is color-coded in all panels. Projections of the particles' trajectories in each orthogonal plane are shown in light blue in the left panels, and the projection in x–z in the middle panels.

4. Discussion and Conclusions

We find that it is possible to produce a suprathermal PUI tail downstream of the HTS consistent with IBEX observations with a significant level of turbulence at $kR_g \cong 1$. The IBEX proton spectrum is formed by PUIs accelerated in the upstream motional electric field, aided by the presence of turbulence. The level of turbulence power required to produce this suprathermal tail was not directly identified by Voyager 2 in the PUI foot, but was observed at much smaller scales in the shock ramp (Figure 2). It is beyond the scope of this study to determine the origin of the "enhanced" turbulence in the PUI foot (i.e., turbulence power greater than what is determined from Voyager 2 observations). We can only speculate that this enhanced level of turbulence in the PUI foot may be related to shock self-reformation (Lembege et al. 2004), shock front ripples (Umeda et al. 2014) originating from instabilities induced by ion temperature anisotropies (Winske & Quest 1988), cross field currents (Lembege & Savoini 1992), or interplanetary SW turbulence transported through the HTS (Giacalone et al. 2021). Hybrid simulation results by Giacalone et al. (2021) show a suprathermal PUI tail at energies $\gtrsim$2 keV downstream of the HTS in the shock frame. While there are a few differences between our model assumptions, our results show reasonable agreement with Giacalone et al. (2021), but our results suggest that moderately stronger fluctuations at the HTS near $kR_g \cong 1$ are necessary to reproduce IBEX observations.

The IHS proton spectral slope appears to steepen as a function of angle in the sky away from the nose (Figure 3(a); Zirnstein et al. 2021). We do not expect the steepening of the proton spectrum to be caused by time dependence, since the observations were time averaged from 2009–2016. A detailed analysis of the origin of a steeper proton spectrum is beyond the scope of this study, but we speculate it may be related to (1) a decrease in HTS compression ratio and/or turbulence power, (2) a more oblique shock, or (3) PUI adiabatic cooling in the heliosheath.

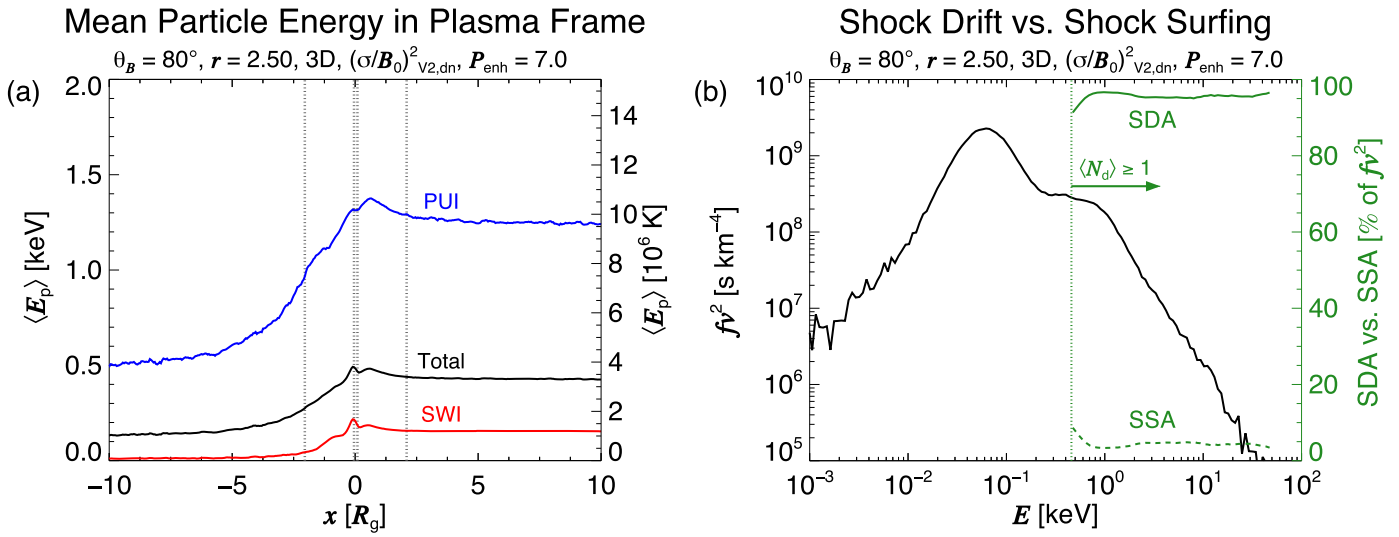

Figure 5. (a) Mean particle energy in the plasma frame as a function of distance along the shock normal. (b) Relative contribution of shock drift acceleration (SDA) and shock surfing acceleration (SSA) mechanisms to the downstream proton distribution.

The source of ENAs observed by IBEX from a particular direction in the sky is spread over a large distance in the IHS. Our analysis does not consider possible changes to the proton distribution downstream of the HTS as it advects through the IHS. A thorough discussion of PUI heating at shocks or turbulence in the IHS is beyond the scope of this work. Here, we consider the effects of charge-exchange and adiabatic heating in the context of a global MHD model.

First, charge-exchange is an energy-dependent process. Higher-energy protons experience charge-exchange more frequently (only up to ∼20 keV; Lindsay & Stebbings 2005); therefore, the proton distribution at IBEX energies may "cool" over time (Schwadron et al. 2014). We estimated the effects of charge-exchange on the IBEX data in this study using the heliosphere simulation from Zirnstein et al. (2021). We calculated the rate of charge-exchange for protons within each IBEX-Hi passband in the plasma frame along streamlines intersecting the Voyager 2 direction and found that the IBEX proton fluxes should be ∼50% higher at the HTS. Interestingly, the difference between IBEX-Hi passbands 2 and 6 (central energies ∼0.9 and 4.7 keV in the plasma frame) is only a few percent.

Second, the proton distribution may undergo compression and adiabatic heating in the IHS. We estimated the effects of adiabatic heating by calculating the mean change in plasma density along streamlines from the HTS that intersect the Voyager 2 direction in the heliosphere simulation. The plasma density changes on average by only a few percent, and therefore has little effect on the IBEX proton spectrum.

Thus, the slope of the IBEX proton spectrum is not significantly modified by charge-exchange or adiabatic heating, at least according to our global, steady-state heliosphere simulation. If charge-exchange is the dominant process affecting the evolution of ∼1–10 keV PUIs in the IHS, then the observed fluxes shown in Figures 3 and 4 should be ∼50% higher. Our model results would underestimate the modified flux, but this can easily be fixed if (1) the CSP energy or shock compression ratio are slightly higher and/or (2) the average IHS thickness during 2009–2016 is greater than 35 au, as is suggested by most global heliosphere models.

This work was funded by the IBEX mission as a part of the NASA Explorer Program (80NSSC20K0719) and the IMAP mission as a part of NASA's Solar Terrestrial Probes mission line (80GSFC19C0027). E.Z. acknowledges support from NASA grant 80NSSC20K0783. R.K. was partially supported by the Max-Planck/Princeton Center for Plasma Physics. The authors thank Len Burlaga and Jamie Rankin for providing Voyager 2 0.48 s magnetic field data, and helpful discussions with Pawel Swaczyna. The work reported in this Letter was performed at the TIGRESS high-performance computer center at Princeton University, which is jointly supported by the Princeton Institute for Computational Science and Engineering and the Princeton University Office of Information Technology's Research Computing department.

Appendix A
Mean and Turbulent Magnetic Field

We model the mean magnetic field, $\boldsymbol{B}_0$, by constructing a PUI foot, ramp, overshoot, and downstream region with specified lengths and amplitudes. Some previous studies of test particle acceleration utilize shock profiles extracted directly from PIC simulations (Yang et al. 2009, 2011). We use an analytic function of the mean field as shown below that approximately reproduces Voyager 2 observations of the HTS (Burlaga et al. 2008; Richardson et al. 2008). This method also allows us to vary the shock structure parameters to understand how different sizes of the PUI foot, ramp, and overshoot affect the downstream proton spectrum in the context of IBEX observations. This will be the subject of future studies.

The mean magnetic field magnitude of our model is shown in Figure 1(b), where the angle between $\boldsymbol{B}_0$ and the shock normal is $\theta_B = 80°$ based on Voyager 2 observations of the local mean magnetic field near the HTS (Richardson et al. 2008). We utilize a modified version of the mean magnetic field

profile from Ariad & Gedalin (2013), given as

$$\begin{aligned}
\boldsymbol{B}_{0,x} &= B_{0,u}\cos(\theta_B),\\
\boldsymbol{B}_{0,y} &= B_{0,u}\sin(\theta_B)\\
&\quad\times\left\{1+\frac{A_{\rm f}-1}{2}\left[1+\tanh\left(\frac{3}{D_{\rm f}}(x+D_{\rm f}-1)\right)\right]\right.\\
&\quad+\frac{A_{\rm ro}-A_{\rm d}}{2}\left[\exp\left(-\frac{2x}{D_{\rm d}}\right)\mathrm{erfc}\left(-\frac{20}{D_{\rm d}}(x-0.3D_{\rm ro})\right)\right]\\
&\quad\left.+\frac{A_{\rm d}-A_{\rm f}}{2}\left[1+\tanh\left(\frac{3}{D_{\rm ro}}x\right)\right]\right\},\\
\boldsymbol{B}_{0,z} &= 0.
\end{aligned} \tag{A1}$$

The mean field HTS structure is constructed with three components: PUI foot ($A_{\rm f}=2.05$, $D_{\rm f}=2R_{\rm g}$), ramp + overshoot ($A_{\rm ro}=5.75$, $D_{\rm ro}=1R_{\rm i}$), and downstream ($A_{\rm d}=r$, $D_{\rm d}=1R_{\rm g}$), where $R_{\rm i}$ is the upstream ion inertial length ($R_{\rm i}\cong 0.1R_{\rm g}$) and $r=2.5$ is the compression ratio. The ramp width is $1.5R_{\rm i}$, similar to Voyager 2 observations (Burlaga et al. 2008) and PIC simulations (Yang et al. 2015; Kumar et al. 2018). We assume that the bulk flow velocity $\boldsymbol{u}$ is along $+x$ and its magnitude scales inversely with $B_{0,y}$, i.e., $u_x = u_u(B_{0,u,y}/B_{0,y})$.

The primary motivation for using a test particle model to analyze PUI acceleration at the HTS is the ability to superpose synthetic turbulence on a mean magnetic field of our choice. While our method does not self-consistently develop turbulent fluctuations like PIC simulations, some PIC simulations are not currently able to develop turbulence at the HTS strong enough to accelerate PUIs to energies above ~2 keV (see Figure 3 in Kumar et al. 2018), which may be due to limitations on simulation runtime, domain size, or dimensions of solving field gradients. Here, we can construct a synthetic spectrum of turbulence with desired scales and amplitudes to test the effects of turbulence on particle acceleration.

The turbulent magnetic field component, $\delta\boldsymbol{B}$, is constructed by superimposing a large number of plane waves of random polarizations, phases, and wavevector directions (Giacalone & Jokipii 1999) as follows:

$$\delta\boldsymbol{B}(x,y,z) = \sum_{n=1}^{N} A(k_n)\hat{\xi}_n \times \exp\left[i\boldsymbol{k}_n\cdot(\boldsymbol{z}_n' - \boldsymbol{u}t) + i\beta_n\right], \tag{A2}$$

$$\hat{\xi}_n = \cos\alpha_n \boldsymbol{x}_n' \pm i\sin\alpha_n \boldsymbol{y}_n', \tag{A3}$$

$$\begin{pmatrix} x'\\ y'\\ z'\end{pmatrix} = \begin{pmatrix} \cos\theta_n\cos\varphi_n & \cos\theta_n\sin\varphi_n & -\sin\theta_n\\ -\sin\varphi_n & \cos\varphi_n & 0\\ \sin\theta_n\cos\varphi_n & \sin\theta_n\sin\varphi_n & \cos\theta_n\end{pmatrix}\begin{pmatrix} x\\ y\\ z\end{pmatrix}, \tag{A4}$$

where N is the total number of wave modes (chosen such that there are 100 wave modes per decade of logarithmic wavenumber, k_n), α_n is the wave polarization, β_n is the wave phase, θ_n and φ_n are the propagation angles, and $\pm$ in Equation (A3) represents the sign of circular polarization. Equation (A2) includes a term $-\boldsymbol{k}_n\cdot\boldsymbol{u}t$ that simulates the advection of turbulence with the bulk plasma flow velocity $\boldsymbol{u}$ over the particle's lifetime t.

We assume a Kolmogorov power spectrum for turbulence over the spatial scales of interest, such that

$$A^2(k_n) = 2\sigma^2 G(k_n)\Big/\left[\sum_{n=1}^{N} G(k_n)\right], \tag{A5}$$

$$G(k_n) = \frac{\Delta V_n}{1+(k_n L_{\rm c})^{\nu}}, \tag{A6}$$

$$\nu = \begin{cases} 5/3 & (1{\rm D})\\ 8/3 & (2{\rm D})\\ 11/3 & (3{\rm D})\end{cases},\quad \Delta V_n = \begin{cases} \Delta k_n & (1{\rm D})\\ 2\pi\, k_n\Delta k_n & (2{\rm D})\\ 4\pi\, k_n^2\Delta k_n & (3{\rm D})\end{cases}, \tag{A7}$$

where ν is the turbulence spectral index (note that Equation (A5) is properly normalized with a factor of 2; note the typo in Giacalone & Jokipii 1999). The majority of the results presented in this study assume 3D isotropic turbulence, but we also show results using a composition of 1D+2D turbulence, as described in Section 3.1.

We create a synthetic spectrum of turbulence in our model in two steps. First, we initialize a spectrum of background turbulence everywhere in our simulation domain using Equations (A2)–(A7). We initialize waves in the range $0.1/R_g < k < 1000/R_g$, assume the correlation length of the background turbulence is much larger than $10R_{\rm g}$, and the turbulence power spectrum is normalized to be consistent with Voyager 2 downstream observations. Additionally, we use a scaling factor to suppress turbulence upstream of the PUI foot where our model assumes no electric fields. The turbulence components in Equation (A2) are modified as

$$\delta\boldsymbol{B}_{\rm sc}(x,y,z) = \begin{cases} \delta\boldsymbol{B}(x,y,z)\sqrt{|B_{0,y}|/|B_{0,u,y}|-1}, & \text{if } |B_{0,y}/B_{0,u,y}|<1\\ \delta\boldsymbol{B}(x,y,z), & \text{if } |B_{0,y}/B_{0,u,y}|\geqslant 1\end{cases}. \tag{A8}$$

Equation (A8) implies that $(\delta B)^2 = 0$ upstream of the shock foot and $(\delta B)^2 = \sigma^2$ at the start of and beyond the shock ramp. Note that this applies to wavenumbers at all scales.

In the second step, we simulate an enhanced level of turbulence in the PUI foot and ramp of the HTS (and not downstream of the overshoot) by scaling the turbulence power $(\delta B_{\rm sc})^2$ by a factor $P_{\rm enh} > 1$ for all wave modes where $k > 1/R_{\rm g}$. For wave modes $k \leqslant 1/R_{\rm g}$, we assume the ratio $A^2(k_n)/k_n$ from Equation (A5) is constant in order to mimic a turbulence correlation scale at $k = 1/R_{\rm g}$. The enhanced turbulence components can be written as

$$\delta\boldsymbol{B}_{\rm enh}(x,y,z) = \begin{cases} \delta\boldsymbol{B}_{\rm sc}(x,y,z)\sqrt{P_{\rm enh}}, & \text{if } k > 1/R_{\rm g}\\ \delta\boldsymbol{B}_{\rm sc}(x,y,z)\sqrt{P_{\rm enh}(kR_{\rm g})^{5/3}}, & \text{if } k \leqslant 1/R_{\rm g}\\ \delta\boldsymbol{B}_{\rm sc}(x,y,z), & \text{if } P_{\rm enh}(kR_{\rm g})^{5/3} < 1\end{cases}. \tag{A9}$$

The third condition in Equation (A9) requires that $\delta\boldsymbol{B}_{\rm enh} \geqslant \delta\boldsymbol{B}_{\rm sc}$ for wavenumbers smaller than the correlation scale. The turbulent variation in the magnitude of the total magnetic field $\boldsymbol{B}$ is illustrated in two-dimensional planes in Figures 2(c) and (d).

Appendix B
Cross-shock Potential Energy

The magnetic energy contribution to the CSP (third term in Equation (3)) is calculated directly from our model's total magnetic field. We determine the electron contribution (second term in Equation (3)) from Voyager 2 PLS measurements, which indicate that electrons are not heated significantly across the HTS (Richardson et al. 2008). PIC simulation results agree with this measurement, predicting an increase in electron energy across the shock ramp approximately proportional to the magnetic field (Kumar et al. 2018). Therefore, we assume that the electron temperature scales with the compression of B_y, i.e., $T_e(x) = T_{e,u}(B_y(x)/B_{y,u})$, where $T_{e,u} = 20{,}000$ K. The first term in Equation (3) represents SWI flow deflection. We estimate this contribution by integrating the first term in Equation (3) across the PIC-simulated shock ramp from Kumar et al. (2018), obtaining a value of $\sim$0.1 keV.

For convenience, we assume that the flow deflection term scales proportionally with magnetic field and calculate a scaling term Γ that accounts for the addition of energy by the flow deflection. Thus, we rewrite Equation (3) as

$$e\Phi(x) \cong \Gamma\left(\frac{\gamma}{\gamma - 1}k_B T_e(x) + \frac{B_u}{\mu_0 n_u}(B_y(x) - B_{0,u,y})\right), \quad \text{(B1)}$$

where $\Gamma = 2.71$, such that the peak of the CSP energy at the shock overshoot accounts for flow deflection, electron, and magnetic energy. Using Equation (B1), we determine that the peak CSP energy at the shock overshoot (ignoring δB in this example) is $\sim$0.16 keV, which is approximately 1/3 of the upstream flow kinetic energy (see Figure 1(b)).

Appendix C
Particle Initialization and Binning

We initialize particles randomly in an upstream fluid parcel that extends from –4 R_g (hereafter called D_{b1}, initially closest to the shock) to –154 R_g (hereafter called D_{b2}, initially farthest from the shock) along the x-axis in the shock/simulation frame. In the upstream frame, the shock plows through this fluid parcel along the x-axis from the right (see orientation in Figure 1). The distribution function near the edges of the dynamically evolving fluid parcel, when encountered by the shock, differ from the upstream distribution function since the continuity equations are not satisfied near the edges. Therefore, we mitigate this issue by (1) reflecting particles from the upstream-most edge of the fluid parcel in the plasma frame (D_{b2}), and (2) excluding particles from our analysis that are too close to the edges of the fluid parcel.

In practice, the model is solved in the shock frame where the particles and the fluid parcel boundaries are advected with the prescribed bulk flow velocity $u(x)$. Particle binning begins when the fluid parcel edge that is initially closest to the shock (D_{b1}) reaches 25 R_g downstream of the shock overshoot, and binning ends when the fluid parcel edge that is initially farthest from the shock (D_{b2}) is within 5 R_g of the PUI foot. During the binning stage, particles that fall within $5\ R_g < x < 15\ R_g$ are binned each time step into the downstream distribution. The average simulation time is $\sim 17\Omega_g^{-1}$, where Ω_g is the upstream advective ion gyrofrequency.

Finally, we note that the fluid parcel is initialized over large distances in the y and z directions ($|y| < 75\ R_g$ and $|z| < 75\ R_g$) such that particles experience turbulence at scales much larger than the largest turbulence wavelength in the model.

ORCID iDs

E. J. Zirnstein https://orcid.org/0000-0001-7240-0618
R. Kumar https://orcid.org/0000-0003-1925-8469
R. Bandyopadhyay https://orcid.org/0000-0002-6962-0959
M. A. Dayeh https://orcid.org/0000-0001-9323-1200
J. Heerikhuisen https://orcid.org/0000-0001-7867-3633
D. J. McComas https://orcid.org/0000-0001-6160-1158

References

Ariad, D., & Gedalin, M. 2013, JGRA, 118, 2854
Armstrong, T. P., Pesses, M. E., & Decker, R. B. 1985, GMS, 35, 271
Bieber, J. W., Wanner, W., & Matthaeus, W. H. 1996, JGR, 101, 2511
Burlaga, L. F., Ness, N. F., Acuña, M. H., et al. 2008, Natur, 454, 75
Chalov, S. V. 2005, AdSpR, 35, 2106
Decker, R. B., Krimigis, S. M., Roelof, E. C., et al. 2008, Natur, 454, 67
Desai, M. I., Dayeh, M. A., Allegrini, F., et al. 2019, ApJ, 875, 91
Fahr, H.-J., & Siewert, M. 2013, A&A, 558, A41
Giacalone, J., & Decker, R. 2010, ApJ, 710, 91
Giacalone, J., & Jokipii, J. R. 1999, ApJ, 520, 204
Giacalone, J., Nakanotani, M., Zank, G. P., et al. 2021, ApJ, 911, 27
Heerikhuisen, J., Gamayunov, K. V., Zirnstein, E. J., & Pogorelov, N. V. 2016, ApJ, 831, 137
Isenberg, P. A. 2005, ApJ, 623, 502
Kolmogorov, A. 1941, DoSSR, 30, 301
Kumar, R., Zirnstein, E. J., & Spitkovsky, A. 2018, ApJ, 860, 156
Lembege, B., Giacalone, J., Scholer, M., et al. 2004, SSRv, 110, 161
Lembege, B., & Savoini, P. 1992, PhFlB, 4, 3533
Lembège, B., & Yang, Z. 2016, ApJ, 827, 73
Leroy, M. M. 1983, PhFl, 26, 2742
Lever, E. L., Quest, K. B., & Shapiro, V. D. 2001, GeoRL, 28, 1367
Lindsay, B. G., & Stebbings, R. F. 2005, JGR, 110, A12213
Livadiotis, G., McComas, D. J., Schwadron, N. A., Funsten, H. O., & Fuselier, S. A. 2013, ApJ, 762, 134
Matsukiyo, S., & Scholer, M. 2014, JGRA, 119, 2388
Matthaeus, W. H., & Goldstein, M. L. 1982, JGR, 87, 6011
Matthaeus, W. H., Goldstein, M. L., & Roberts, D. A. 1990, JGR, 95, 20673
McComas, D. J., Allegrini, F., Bochsler, P., et al. 2009, Sci, 326, 959
McComas, D. J., Bzowski, M., Dayeh, M. A., et al. 2020, ApJS, 248, 26
McComas, D. J., & Schwadron, N. A. 2006, GeoRL, 33, L04102
McComas, D. J., Swaczyna, P., Szalay, J. R., et al. 2021, ApJS, 254, 19
McComas, D. J., Zirnstein, E. J., Bzowski, M., et al. 2017, ApJS, 233, 8
Mostafavi, P., Zank, G. P., Zirnstein, E. J., & McComas, D. J. 2019, ApJL, 878, L24
Parker, E. N. 1958, ApJ, 128, 664
Press, W. H., Teukolsky, S. A., Vetterling, W. T., & Flannery, B. P. 2002, Numerical Recipes in C: The Art of Scientific Computing (2nd ed.; Cambridge: Cambridge Univ. Press)
Reisenfeld, D. B., Bzowski, M., Funsten, H. O., et al. 2019, ApJ, 879, 1
Richardson, J. D., Kasper, J. C., Wang, C., Belcher, J. W., & Lazarus, A. J. 2008, Natur, 454, 63
Richardson, J. D., & Smith, C. W. 2003, GeoRL, 30, 1206
Schwadron, N. A., Moebius, E., Fuselier, S. A., et al. 2014, ApJS, 215, 13
Senanayake, U. K., & Florinski, V. 2013, ApJ, 778, 122
Stone, E. C., Cummings, A. C., Heikkila, B. C., & Lal, N. 2019, NatAs, 3, 1013
Swaczyna, P., McComas, D. J., Zirnstein, E. J., et al. 2020, ApJ, 903, 48
Umeda, T., Kidani, Y., Matsukiyo, S., & Yamazaki, R. 2014, PhPl, 21, 022102
Winske, D., & Quest, K. B. 1988, JGR, 93, 9681
Yang, Z., Liu, Y. D., Richardson, J. D., et al. 2015, ApJ, 809, 28
Yang, Z. W., Lembège, B., & Lu, Q. M. 2011, JGRA, 116, A08216
Yang, Z. W., Lu, Q. M., Lembège, B., & Wang, S. 2009, JGRA, 114, A03111
Zank, G. P., Adhikari, L., Zhao, L.-L., et al. 2018, ApJ, 869, 23
Zank, G. P., Pauls, H. L., Cairns, I. H., & Webb, G. M. 1996, JGR, 101, 457
Zirnstein, E. J., Dayeh, M. A., Heerikhuisen, J., McComas, D. J., & Swaczyna, P. 2021, ApJS, 252, 26
Zirnstein, E. J., Giacalone, J., Kumar, R., et al. 2020, ApJ, 888, 29
Zirnstein, E. J., Kumar, R., Heerikhuisen, J., McComas, D. J., & Galli, A. 2018a, ApJ, 860, 170
Zirnstein, E. J., & McComas, D. J. 2015, ApJ, 815, 31
Zirnstein, E. J., McComas, D. J., Kumar, R., et al. 2018b, PhRvL, 121, 075102